Single-atom Co-N-C catalysts for high-efficiency reverse water-gas shift reaction

Yihui Li [a,c,1], Ziang Zhao [a,1], Wei Lu [a], Hejun Zhu [a,*], Fanfei Sun [e], Bingbao Mei [e], Zheng Jiang [e], Yuan Lyu [a], Xingkun Chen [d], Luyao Guo [a,d], Tong Wu [a,f], Xinzheng Ma [a,d], Yu Meng [g,*], Yunjie Ding [a,b,d,**]

[a] Dalian National Laboratory for Clean Energy, Dalian Institute of Chemical Physics, Chinese Academy of Sciences, Dalian 116023, PR China
[b] State Key Laboratory of Catalysis, Dalian Institute of Chemical Physics, Chinese Academy of Sciences, Dalian 116023, PR China
[c] University of Chinese Academy of Sciences, Beijing 100049, PR China
[d] Hangzhou Institute of Advanced Studies, Zhejiang Normal University, Hangzhou 311231, PR China
[e] Shanghai Synchrotron Radiation Facility, Shanghai Institute of Applied Physics, Chinese Academy of Sciences, Shanghai 201204, PR China
[f] State Key Laboratory of Fine Chemicals and School of Chemical Engineering, Dalian University of Technology, Dalian 116024, PR China
[g] Shaanxi Key Laboratory of Low Metamorphic Coal Clean Utilization, School of Chemistry and Chemical Engineering, Yulin University, Yulin 719000, PR China

ARTICLE INFO

ABSTRACT

Designing efficient non-precious metal catalysts for CO_2 hydrogenation is a significant challenge. Cobalt-based catalysts often failed to catalyze the reverse water-gas shift (RWGS) reaction with high CO selectivity and stability. Herein, nitrogen-doped carbon (N-C) immobilized single-atom $Co-N_4$ catalyst with 5% Co loading were prepared by anchoring strategy through regulating the cobalt species coordination structure. The stable single-atom catalyst achieves almost 100% CO selectivity and a high CO_2 conversion of 52.4% at 500 °C during CO_2 hydrogenation, while the 20% Co-N-C nanoparticle catalyst favored CH_4 formation. The experiments and density functional theory (DFT) calculations revealed that atomically dispersed $Co-N_4$ site followed the hydrogen-assisted pathway in which the intermediate COOH* was desorbed and dissociated into CO, whereas the Co nanoparticle catalysts mainly followed the direct dissociation. This study provided a new strategy for designing Co-based RWGS catalysts with excellent performance.

1. Introduction

As a major greenhouse gas, CO_2 is also an abundant carbon source [1, 2], and its capture and utilization (CCU) has been considered an economically viable measure [3–6]. CO_2 hydrogenation into CO and H_2O, known as the reverse water-gas shift (RWGS) reaction [7–9], has received extensive attention for the reason that CO is an important feedstock for the production of clean liquid fuels and value-added chemicals via Fischer-Tropsch synthesis (FTS) [7,10–14]. Accordingly, the production of CO from captured CO_2 is a vital step in the carbon cycle [15,16]. In particular, it is more economical and practical to utilize cheaply green H_2 from solar, wind recyclable and nuclear energy.

Owing to the complexity of the CO_2 hydrogenation reaction network [17], understanding the origin of CO_2 selective hydrogenation is vital for reasonable design of catalysts with high catalytic activity and desired selectivity. Usually, the production of CO through CO_2 hydrogenation reaction is accompanied by the formation of methane, which is complex and energy-intensive to separate in spite of its high utilization value [18, 19]. Uncovering the origin of tunable the selectivity towards CO and CH_4 is important for the rational design of CO_2 hydrogenation catalysts [20,21]. It has been proposed that CO_2 hydrogenation is a structure sensitive reaction, which means that not all surface atoms on the supported metal catalysts have the same activity [22–25]. Various factors such as crystal structure, particle size [26,27], carrier interactions [28], and active metals have all been shown to affect catalytic performance.

Although great achievement, especially in the Pt-based noble metal

catalyst, have been made for selective CO_2 hydrogenation to CO [15,21, 29], the design and synthesis preparation of cheap and efficient catalysts remain a research hotspot for CO_2 hydrogenation. Non-precious metal Co is an interesting candidate worth investigating for CO_2 hydrogenation because of its high CO dissociation and C-C coupling ability in CO hydrogenation reaction [30]. Unfortunately, Co-based nanoparticle catalysts generally exhibit low CO selectivity in CO_2 hydrogenation [23] and are more likely to promote the hydrogenation of adsorbed CO* to methane [31]. For instance, Co-based nanoparticle sites generally exhibit striking methane selectivity, such as Co/ZrO_2 [32], Co/TiO_2 [33] and Co/CeO_2 catalysts [34].

Recently, single-atom Co based catalysts have been synthesized to enhance CO selectivity in CO_2 hydrogenation. H. Liang and co-workers have reported that the Co/SBA-15 catalysts with stable single-atom Co through Co-O-Si bonds exhibited almost 100% CO selectivity during hydrogenation [35]. The single-atom Co/ZrO_2 catalysts with inherent oxygen vacancies was disclosed to display good 95% CO selectivity in CO_2 hydrogenation reaction [36]. It is desirable to precisely control the uniformity and stability of single-atom Co to achieve an excellent CO selectivity and a high CO_2 conversion at high temperature due to the strong inclination of migration and aggregation of metal atoms.

Herein, we synthesized single-atom Co-N-C catalysts for RWGS reaction using nitrogen-doped carbon (N-C) support through anchoring strategy by tuning the coordination state of Co with N atoms. Coordination by adding highly functionalized carbon supports and chelating agents, followed by nitrogen addition to effectively anchor and stabilize single-atom metals, could tune the electronic state of metal and optimize the intermediates adsorption/desorption. The Co-N-C catalysts were easier to scale up production and metal recovery. The $Co-N_4$ single-atom catalyst with 5% loading (5% Co-N-C catalyst) could reach almost 100% CO selectivity with 52.4% CO_2 conversion (close to the equilibrium conversion) at 500 °C and have excellent stability. With increasing the content of Co to prepare 20% Co-N-C catalyst, the N atoms could not effectively stabilize the Co atoms, leading to the Co species agglomeration into nanoparticle, which was accompanied by the CH_4 generation in CO_2 hydrogenation reaction. Our study provided a novel way to design non-precious metal Co-based catalysts with excellent CO selectivity for CO_2 hydrogenation reaction.

2. Experimental

2.1. Catalysts preparation

2.1.1. Co-N-C with different Co loadings

0.1–2.5 g of $Co(NO_3)_2 \cdot 6\,H_2O$ and 4.8 g of α-D-glucose were dissolved in 20 mL of ultrapure water. Then added 240 mg of carbon supports (Oxygen-functionalized activated carbon) and sonicated for 30 min. After sonication, 35 g of melamine was added to the resulting clear solution and stirred for 1 h, then washed with ultrapure water 2–3 times, and dried at 60 °C for 12 h. The obtained powder was subsequently heated to 800 °C at 10 °C/min under Ar flow. After pyrolysis for 2 h, black Co-N-C catalysts were obtained. The catalysts have different Co loadings according to the content of precursor and Co loadings were determined by Inductively Coupled Plasma (ICP) method.

2.2. Catalyst characterization

2.2.1. Structural characterization

The texture of the catalysts measured by **N_2 physisorption** using Quantachrome Autosorb instrument. 50 mg catalyst was added to a sample tube, degassed at 200 °C for 6 h, and then analyzed in a N_2 atmosphere at − 196 °C. Elemental content testing of samples by **Inductively Coupled Plasma (ICP)** technique on the Perkin Elmer ICP-OES 7300DV equipment. The content of N element of samples was determined by EMGA-930 **ONH elemental analyzer** equipment. **X-ray diffraction spectra (XRD)** was measured by a PANalytical X′Pert3

powder diffractometer with CuKα radiation. Spectra were recorded from 30° to 80° at a scan speed of 2°/min. **High-angle annular dark-field scanning electron microscopy (HAADF-STEM)** was tested on a JEM-ARM200F STEM/TEM instrument, calibrated using a CEOS probe, with an instrument resolution of 0.08 nm and an accelerating voltage of 200 kV. **Raman** spectral characterization was performed using a Bruker Optics Senterra Raman confocal microscope spectrometer with an excitation wavelength of 532 nm. **X-ray photoelectron spectroscopy (XPS)** of the samples was measured using a Thermos Scientific Escalab 250Xi instrument. The electronic states and surface composition of the samples were measured using monochromatic Al Kα at 15KV. **X-ray absorption fine structure (XAFS)** test of the sample was carried out at the BL4W XAFS line station of the Shanghai Synchrotron Radiation Light Source (SSRF), and the test was conducted in a see-through mode. The K-edge energy of metallic Co is 7712 eV [37].

2.2.2. Chemisorption experiment and infrared spectroscopy characterization

The samples were tested for **CO temperature programmed desorption (CO-TPD)** using Zeton Altramira AMI-300 instrument with 100 mg of sample loaded into a U-shaped sample tube. Each sample was purged under Ar atmosphere at 120 °C for 30 min to remove moisture, followed by pulsed CO chemisorption at 50 °C to adsorption saturation, then changed to Ar and held for 30 min. The CO-TPD test was imposed by heating from 50 °C to 800 °C with a ramp of 10 °C/min, and the desorption products were tracked and detected by a Swiss OminiStar 300 mass spectrometer. **H_2-D_2 exchange experiments** was performed on an Autochem II 2920 chemisorption equipped with a mass spectrometer. 50 mg catalyst was loaded into sample tube, pretreated under an Ar atmosphere at 120 °C for 1 h, and then cooled to room temperature. When the baseline was stable, the treatment gas was switched to H_2/D_2 mixture, and the temperature was increased to 250 °C with a ramp of 3 °C/min, and the gas flow was controlled to 15 mL H_2/16 mL D_2. Changes in gas phase components (H_2, D_2, HD) were monitored in real time using mass spectrometry. **Temperature-programmed surface reaction (TPSR)** was performed on Zeton Altramira AMI-300 instrument with a mass spectrometer. 100 mg fresh sample was put into a sample tube, and Ar was first purged at 120 °C for 30 min, and then pass a mixed gas (10% CO/He or 10% CO_2/He or 10% H_2/Ar) to 10°/min heated to 400 °C for testing. The product was monitored in real time by mass spectrometry.

In situ diffuse reflection infrared Fourier transform infrared spectroscopy (DRIFTS) experiments were performed on the VERTEX 80 V FTIR spectrometer. For the in-situ DRIFTS experiments of the RWGS reaction, the sample was first purged in an Ar stream at 120 °C for 30 min, then a stream of gas mixture ($H_2/CO_2/N_2$ =72/18/10) was introduced into the system, and the temperature started to increase until 500 °C.

2.3. Catalytic performance test

The prepared catalysts were evaluated in a fixed-bed plug-flow reactor (inner diameter is 9 mm) for CO_2 hydrogenation reaction. In each evaluation experiment, the reactor was filled with 0.65 g catalyst, and then mixed gas with different ratios of $H_2/CO_2/N_2$ was introduced, in which N_2 was used as the internal standard gas. At atmospheric pressure, the reaction was carried out from room temperature to the corresponding reaction temperature at a ramp of 3 °C/min. The outlet exhaust gas was analyzed online using an Agilent 7890 N GC chromatograph equipped with thermal conductivity detector (TCD) and TDX-01 column. The CO_2 conversion, turnover frequency (TOF), product selectivity, yield and space time yield (STY) were calculated by the internal standard method. The calculated carbon balance is kept above 100% ± 5% and the specific calculation formula is as follows.

$$CO_2 \; Conversion \; (\%) \; = \frac{nCO_{2,in} - nCO_{2,out}}{nCO_{2,in}} \times 100\%$$

$$CO \; Selectivity \; (\%) \; = \frac{nCO_{,out}}{nCO_{,out} + nCH_4} \times 100\%$$

$$CH_4 \; Selectivity \; (\%) \; = \frac{nCH_{4,out}}{nCO_{,out} + nCH_{4,out}} \times 100\%$$

$$Product \; Yield = Product \; Selectivity(\%) \times CO_2 \; Conversion(\%)$$

$$Product \; STY = \frac{nProduct_{,out}}{mCat. \times time}$$

2.4. Theoretical methods

In this work, all the theoretical calculation work was completed by the Vienna Ab Initio Simulation Package (VASP) software [38], which uses the projected augment plane-wave (PAW) [39] pseudopotential method. The cut-off energy was tested and 400 eV was chosen. Each element adopts the standard pseudopotential of the PBE method [40]. Considering that the Co-based catalyst is a magnetic system, spin polarization is used in all calculations, which is helpful to predict the electronic properties of magnetic materials more accurately[41]. For structural optimization and property calculation, the convergence criteria of force and energy are set as 0.02 eV/A and 10–5 eV, respectively, and Gaussian method of 0.05 eV electron broadening was applied. The climbing image nudged elastic band (CI-NEB) method [42] was used to search each transition state, and the frequency calculation was used to confirm whether the transition state was correct.

The calculated structural models of 5% and 20% Co loading catalysts were simulated by N-doped graphene loaded single atomic Co and metal Co (111) surface, respectively. The specific structural models are shown in Fig. S8. For each structural model, the sampling density of K-point in Brillouin zone was 0.04 2 * π/Angstrom. By testing, the energy converges to the sampling density of this K-point.

3. Results and discussion

3.1. Structure analysis of catalysts

Co-N-C single-atom catalysts (SAC) was prepared using the anchoring strategy by multi-step ultrasonic mixing of glucose, modified activated carbon, melamine and cobalt nitrate, followed by pyrolysis under argon atmosphere, like an earlier report by Zhao et al. [43] The
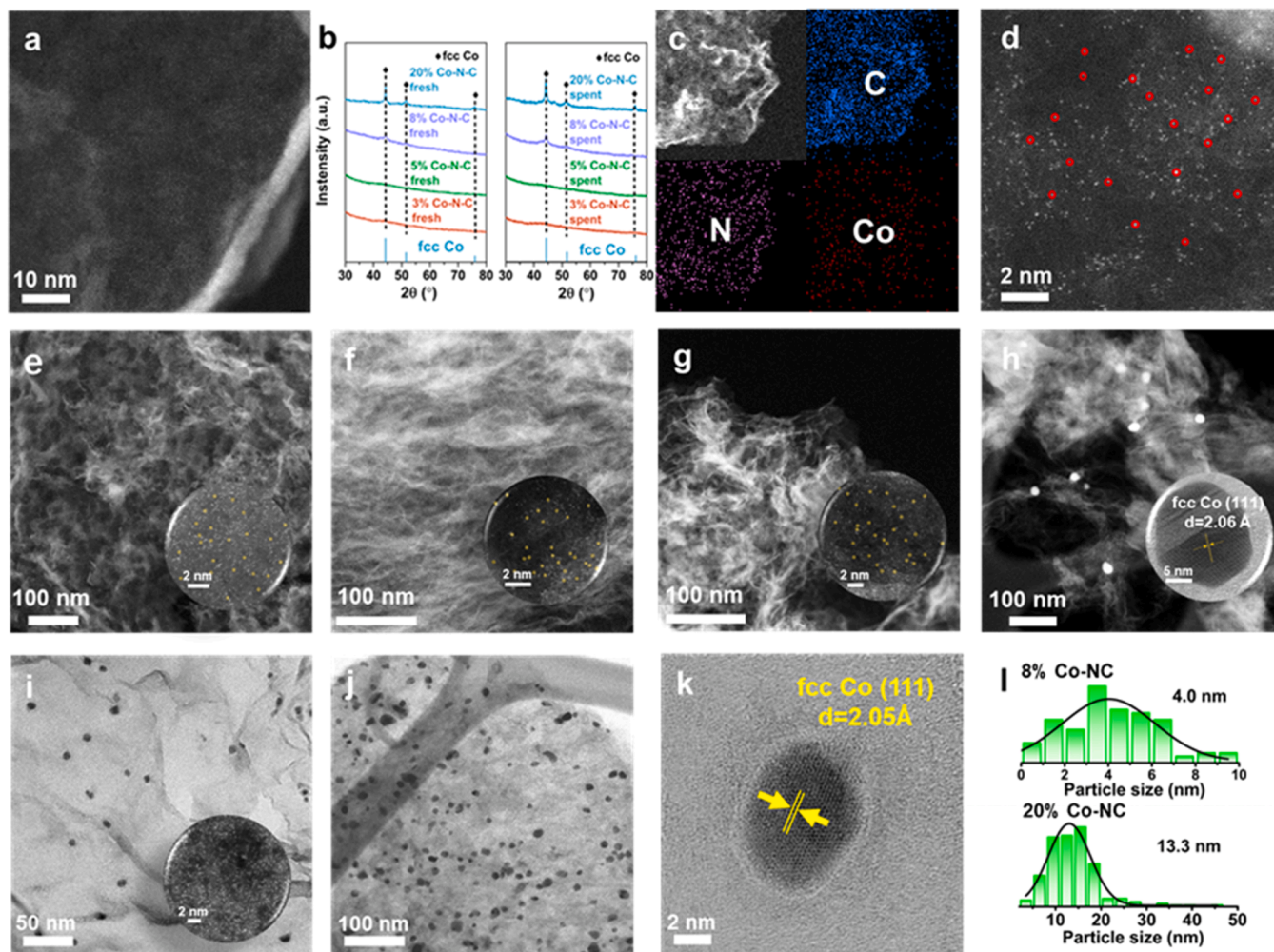

Fig. 1. Structural characterizations over the Co-N-C catalysts. (a) HAADF-STEM image of the 5% Co-N-C catalyst at low magnification. (b) XRD patterns of the Co-N-C catalyst with different Co loadings. (c) HAADF-STEM and EDX-mapping images of Co, N and C on 5% Co-N-C catalyst. (d) HAADF-STEM image of the 5% Co-N-C catalyst. (e-h) HAADF-STEM images of the 5% Co-N-C catalyst after CO_2 hydrogenation at (e) 300 °C, (f) 400 °C, (g) 500 °C and (h) 600 °C. (i) TEM and HAADF-STEM images of the 8% Co-N-C catalyst. (j) TEM image of the 20% Co-N-C catalyst. (k) Lattice fringes of Co nanoparticles on the 20% Co-N-C catalyst. (l) Particle distribution over the 8% Co-N-C and 20% Co-N-C catalysts, respectively.

metal cobalt ions were first efficiently segregated by glucose chelation, then anchored onto functional group-rich activated carbon supports by O-functional group interaction. Subsequently, excessive amounts of melamine were added as the nitrogen source. During the pyrolysis process, glucose first decomposed into carbon residues at lower temperature to isolate the metal cobalt. The melamine firstly underwent condensation and polymerization reactions to form an N-doped carbon with temperature rising, which could capture the Co atoms to form atomically dispersion in the case of the N content higher than the Co loading (Table S1) on the 3% and 5% Co-N-C catalysts. With the increase of Co loading higher than the N content (Table S1), 8% and 20% Co-N-C catalysts containing Co nanoparticle (NP) were prepared to explore the role of Co species dispersion in RWGS reaction.

HAADF-STEM was used to obtain evidence of Co distribution at atomic resolution. It can be clearly observed that the bright spots with single-atom sites are uniformly dispersed on the 5% Co-N-C catalyst, which can be attributed to single-atom Co (Fig. 1a, d and Fig. S1), whereas agglomerated crystalline Co nanoparticles were found on the 8% Co-N-C and 20% Co-N-C catalysts, and the lattice fringes of fcc-Co (111) plane (d=2.05 Å) were observed at low magnification (Fig. 1i, j and k),which is consistent with XRD patterns [44]. In addition, atomically dispersed Co species were also found on 8% Co-N-C catalyst (Fig. 1i), indicating that the agglomeration of Co species was not complete. It implied that carbon support in the catalysts worked as a reductant to reduce Co oxides during carbonization process. However, as for 3% Co-N-C and 5% Co-N-C catalysts, the diffraction peaks related with Co species were not detected in XRD patterns (Fig. 1b). From the particle size analysis of TEM micrographs (Fig. 1l), the average particle size of 8% Co-N-C and 20% Co-N-C were determined to be 4.0 nm and

13.3 nm, respectively, which showed same trend as the XRD results (Table S1). Scanning Transmission Electron Microscopy coupled with Energy Dispersive Spectroscopy (STEM-EDS) images displayed that Co, C and N were uniformly dispersed on the 5% Co-N-C catalyst (Fig. 1c). The Raman spectrum (Fig. 2b) only showed that D (disordered carbon) and G (graphite) bands were observed on the catalysts.

XPS and XAFS characterizations were conducted to highly sensitive determine the chemical state and coordination environment of Co-N-C catalysts. As shown in Fig. 2c, it was found that the Co $2p_{3/2}$ binding energy was in the range of 781.3–781.7 eV, mainly the characteristic binding energy peak of the Co^{2+} on the 3% Co-N-C and 5% Co-N-C catalysts, whereas the Co^0 peaks appeared (778.2 eV) on the 8% Co-N-C and 20% Co-N-C catalysts and with the increase of loading, the peak of Co^0 is obviously enhanced. The N 1 s XPS spectra could be deconvoluted into five different N species: pyridinic N (398.0 eV), Co-N (399.5 eV), pyrrolic N (400.5 eV), graphitic N (401.3 eV) and oxidized graphitic N (403.0 eV) (Fig. S2) [45]. Pyrrolic-N and pyridinic-N were the predominant N species in the 5% Co-N-C catalyst. These two N species likely promoted the stabilization of atomic Co sites by coordination with the metal. As shown in Fig. 2f, the X-ray absorption near edge structure (XANES) spectra of the fresh and spent 5% Co-N-C catalysts were similar. The XANES spectra of the fresh and spent 20% Co-N-C catalysts were like metallic Co foils in Fig. 2g. Fig. 2d and e showed the Fourier transform (FT) k^3-weighted extended X-ray absorption fine structure (EXAFS) spectrum of the Co k-edge. Compared with Co foil, no obvious peak of Co-Co coordination was observed in the 5% Co-N-C catalysts. And the FT EXAFS spectrum of the 5% Co-N-C catalyst had a strong peak at 1.50 Å, which could be well attributed to the Co-N distance, where the nitrogen shell surrounded Co single atom.
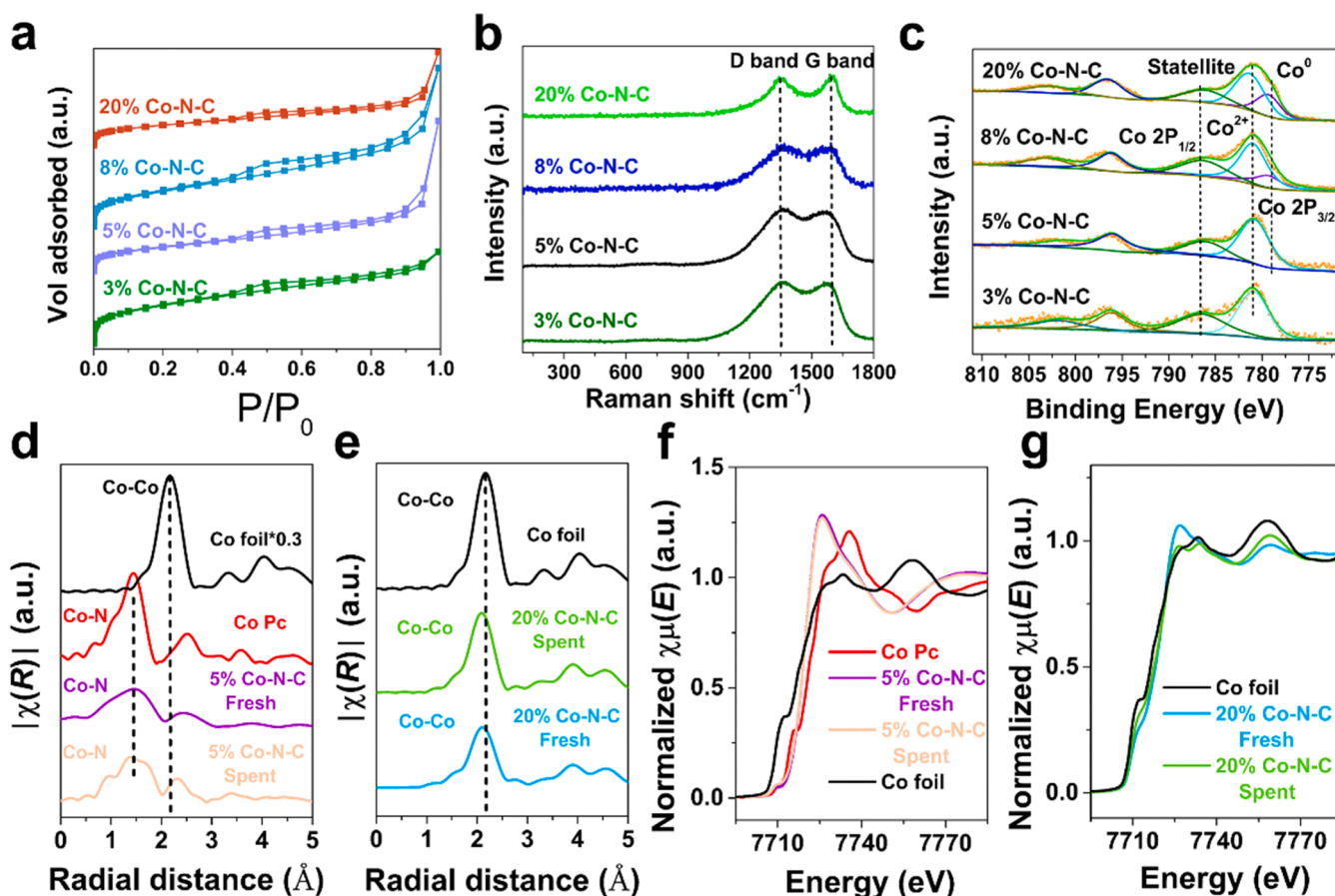

Fig. 2. Structural characterizations and atomic structure analysis over the Co-N-C catalysts. (a) N₂ adsorption/desorption isotherm of Co-N-C catalysts. (b) Raman spectra of the fresh Co-N-C catalysts. (c) Co 2p XPS analysis for the spent Co-N-C catalysts. (d. e) EXAFS and (f. g) XANES of Co K-edge for the fresh and spent 5% Co-N-C and 20% Co-N-C catalysts. Reference materials: Co foil, Co Pc (cobalt phthalocyanine).

Combined with the above HAADF-STEM results, all the Co species in the fresh and spent 5% Co N-C catalysts were atomically dispersed. To obtain further insight into the chemical configuration of Co species, FT EXAFS fittings were performed in r, q, and k spaces to reveal structural parameters and evaluate fitting quality. As shown in Fig. S3, all fittings agreed with the experimental data, providing an average coordination number of the first shell (Co-N) of 4.0 ± 0.2 and an average Co-N bond length of 1.97 ± 0.03 Å of 5% Co-N-C catalyst (Table S3). Therefore, the 5% Co-N-C catalyst had a $Co-N_4$ coordination structure. N/Co mole ratio is 3.1 for the 8% Co-N-C catalyst (Table S1), which is lower than coordination number of 4, indicating that the amount of N atoms was not enough to coordinate and anchor all of Co species as Co atoms and thus partial Co species agglomerated into Co nanoparticles. As Co content further increase to 20% loading, the N/Co mole ratio of 0.8 (Table S1) is too low to enable N stabilizing Co atoms, leading to formation of the Co nanoparticles.

3.2. CO_2 hydrogenation performance

The steady-state catalytic performance of the Co-N-C catalysts with different dispersed state of Co species for CO_2 hydrogenation reaction was evaluated, as shown in Fig. 3. CO and CH_4 were the detectable products for all the catalysts. As shown in Fig. 3a, CO_2 conversion increased with the elevated Co loadings and dispersion state of Co species was crucial for product selectivity. The space time yield (STY) of CO presented a "volcanic" curve with the Co loading increased, but the CH_4 STY increased with the Co loading increased. For the 1% Co-N-C, 3% Co-N-C and 5% Co-N-C atomically dispersed Co catalysts, the CO selectivity can reach up to 99%. The CO STY of 3% Co-N-C catalyst can reach 37.5 $mol·kg^{-1}·h^{-1}$ and the CO yield of 5% Co-N-C catalysts can reach 51.5%, which has significantly improved compared with other Co-based catalysts (Table S4). With the Co species agglomerated from single-atom sites to nanoparticles, the CH_4 selectivity dramatically increased, among which the 8% Co-N-C catalyst had CH_4 formation and the CH_4 selectivity of the 20% Co-N-C catalyst can reach 99.3%, and the CH_4 STY of 20% Co-N-C catalysts can reach 33.6 $mol·kg^{-1}·h^{-1}$ (Table S4). As shown in Fig. 3b, H_2/CO_2 ratio have no obvious effect on the CO selectivity for the 5% Co-N-C catalyst (99.5%−98.3%), but CO_2 conversion increased with elevated H_2/CO_2 ratio. With elevated temperature from 250 °C to 500 °C, CO_2 conversion increased for both 5% Co-N-C and 20% Co-N-C catalysts and the conversion at 500 °C could reach 52.4% and 71.2% (Table S4), respectively, accompanying with the increase of CO selectivity of the 5% Co-N-C catalyst and the almost constant CH_4 selectivity of the 20% Co-N-C catalyst (>95%) (Fig. 3c). To explore the effect of Co loading on the TOF under different reaction temperatures, it was found that 3% Co-N-C catalyst had the highest value 73 h^{-1} of CO_2 to CO TOF. The CO_2 to CH_4 TOF increased firstly with the increase of temperature from 250 °C to 350 °C, and then remained almost unchanged as temperature further increased over the 20% Co-N-C catalyst (Fig. S5). The CO STY of 5% Co-N-C and the CH_4 STY of 20% Co-N-C catalysts increase with increasing temperature, respectively. From the Fig. 3d, the CO_2 conversion decreases but the CO STY increases with increasing weight hourly space velocity (WHSV) for the 5% Co-N-C catalyst. And it was found that the CO selectivity was still as high as 98% even when the WHSV reached up to 72000 $mL·gcat^{-1}·h^{-1}$. Strikingly, the catalytic performance of the RWGS reaction towards the 5% Co-N-C catalyst remained stable at 400 °C for 100 h time on stream (Fig. 3e). No fcc Co characteristic peak was observed in the XRD pattern of the 5% Co-N-C catalyst after 100 h reaction (Fig. S4). The HAADF-STEM characterization of the spent 5% Co-N-C catalyst at different reaction temperatures were shown in Fig. 1e-h. No cobalt agglomeration and lattice fringes were found in this catalyst after the RWGS reaction at 300, 400 and 500 °C. With the temperature further increasing to 600 °C, Co nanoparticle were found after reaction and CH_4 selectivity was significantly increased (Fig. 3f). It indicated that the single-atom catalyst remained stability at 500 °C during the RWGS reaction.

The results showed that the Co-N-C single-atom catalyst mainly works for RWGS reaction with similar CO selectivity at different WHSV and H_2/CO_2 ratios. However, it increased conspicuously as the reaction temperature increased, which was in accordance with the thermodynamic law [6]. When the distribution of Co species changed from single atoms to nanoparticles, the product selectivity changed significantly. The decrease of CO selectivity is accompanied by the increase of CH_4
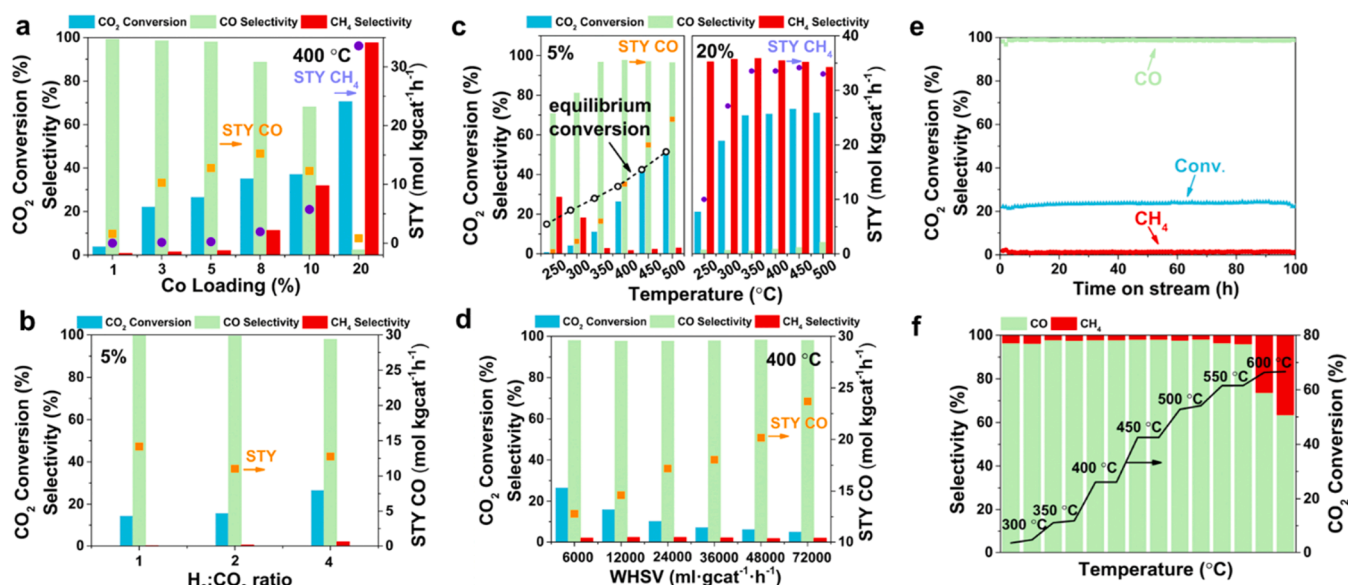

Fig. 3. Catalytic performance of Co-N-C catalysts for CO_2 hydrogenation. CO_2 conversion, product selectivity and space time yield (STY) at different (a) Co loadings (Reaction conditions: 400 °C, 0.1 MPa, 6000 $mL·g^{-1}·h^{-1}$, $H_2/CO_2/N_2$ =72/18/10), (b) H_2: CO_2 ratios (Catalyst: 5% Co-N-C; Reaction conditions: 400 °C, 0.1 MPa, 6000 $mL·g^{-1}·h^{-1}$), (c) Reaction temperatures over the 5% Co-N-C and 20% Co-N-C catalysts (Reaction conditions: 0.1 MPa, 6000 $mL·g^{-1}·h^{-1}$, $H_2/CO_2/N_2$ =72/18/10), (d) WHSV (Catalyst: 5% Co-N-C; Reaction conditions: 400 °C, 0.1 MPa, $H_2/CO_2/N_2$ =72/18/10). (e) 100 h time on stream of the 5% Co-N-C catalyst (Reaction condition: 400 °C, 0.1 MPa, 6000 $mL·g^{-1}·h^{-1}$, $H_2/CO_2/N_2$ =72/18/10). (f) The product selectivity over the 5% Co-N-C catalyst with temperature programmed to 600 °C.

selectivity, and the CH_4 selectivity of the 20% Co-N-C catalyst reach 99.8%. Therefore, single-atom Co species and Co nanoparticles exhibit excellent CO and CH_4 selectivity, respectively. The distribution of Co species played an important role in tuning product selectivity in the CO_2 hydrogenation.

3.3. Proposed reaction network

In order to explore the role of different Co species in the CO_2 hydrogenation reaction process, temperature-programmed experiments were carried out. The CO adsorption performance of the Co-N-C catalysts were estimated through CO-TPD, as shown in Fig. 4a. During the desorption process, the desorbed peaks at 500–600 °C were mainly attributed to the desorption of CO adsorbed on the Co species [46]. It could be observed that there was no CO desorption peak on the 3% Co-N-C and 5% Co-N-C catalyst, and a weak and broad peak at 522 °C existed on the 8% Co-N-C catalyst. The 20% Co-N-C catalyst showed an obvious desorption peak at 529 °C. The above results indicated that larger Co nanoparticles had stronger affinity for CO, and CO was more easily bound to the large Co nanoparticles. However, single-atom Co species has relatively weak CO adsorbed ability. Therefore, the direct desorption of CO is favored over the single-atom Co-N-C catalysts. Then, the H_2-D_2 exchange experiment was used to explore the H_2 activation ability of different Co species [47]. From Fig. 4b, we could find that the starting temperature of HD formation was in the order of 20% Co-N-C < 8% Co-N-C < 5% Co-N-C < 3% Co-N-C. This indicated that the ability to activated H_2, as further hydrogenated to CH_4 [48,49], gradually increased with increase of Co loading. To explore the pathway of CO generation on Co-N-C catalysts, we performed the chemisorption characterization of CO-TPSR and CO-H_2-TPSR (Fig. 4c). It was found that 3% Co-N-C and 5% Co-N-C hardly dissociated CO with the increase of temperature, while 8% Co-N-C and 20% Co-N-C catalysts facilitated CO dissociation under H_2. This indicated that during the reaction, the CO* could also be further consumed on the Co-N-C nanoparticle catalysts surface and the H_2 promoted CO consumption, which was more beneficial for hydrogenation to CH_4. The CO hydrogenation probe reaction was performed on the 20% Co-N-C catalyst, and CH_4 production was found under the same reaction conditions (Fig. S6). The CO_2-TPSR and CO_2-H_2-TPSR of the 5% Co-N-C and 20% Co-N-C catalysts showed that CO and CH_4 generated rapidly after the introduction of H_2, respectively (Fig. S7).

The DRIFTS under RWGS reaction conditions was performed to explore the reaction pathway, as shown in Fig. 5a-d, and the corresponding infrared band assignments were shown in Fig. 5e-j. During the mixed atmosphere (H_2/CO_2/N_2 =72/18/10), two peaks ascribed to gaseous CO at 2111 and 2179 cm^{-1} started to appear on the 5% Co-N-C (Fig. 5a), 8% Co-N-C (Fig. 5b) and 20% Co-N-C (Fig. 5c) catalysts at 250 °C, 350 °C and 450 °C, respectively [50]. Two peaks of gas CH_4 at 1035 and 3017 cm^{-1} started to appear on the 8% Co-N-C and 20% Co-N-C catalysts at 300 °C and 250 °C, respectively. The peaks intensity

increased significantly with elevated temperature, whereas no gaseous CH_4 peaks appeared on the 5% Co-N-C catalyst. This was consistent with evaluation results on each catalyst in Fig. 3a. Moreover, no band assigned to CO* was observed on the 5% Co-N-C catalyst in the temperature range from 250 °C to 500 °C, mainly due to the weak adsorption capacity of single-atom Co for CO (Fig. 5a), which was desorbed on the surface with the formation of CO. The peaks at 1420 and 1650 cm^{-1} correspond to the O-H and the C=O stretching vibration of the COOH* species, respectively. After Ar purging, the COOH* signal became prominent, indicated that COOH* species was the main intermediate over the 5% Co-N-C single atom catalyst during the RWGS reaction (Fig. 5d). The direct dissociation route is generally considered to be the direct dissociation of CO_2 into the CO* intermediate. H-assisted pathway typically involve surface carbonates, formates and acetates as intermediate species. The COOH* species was mainly produced from CO_2 via the H-assisted pathway (Fig. 5k). But for the 8% Co-N-C and 20% Co-N-C catalysts, the CO* linearly adsorbed peak on metallic cobalt could be detected at 2062 and 2066 cm^{-1}, respectively, and the peak of CO* redshifted after the CH_4 appearance. Due to the relatively strong adsorption of CO* on Co nanoparticles, the CO* was hydrogenated to CHO* (1710 cm^{-1}) and CH_2* (1345 cm^{-1}) at elevated temperature until CH_4 was formed. Therefore, CH_4 was more likely formed due to further hydrogenation of CO* directly formed from CO_2. Weckhuysen et al. had demonstrated that metallic cobalt tended to follow the direct dissociation route [34]. Guo et al. also believed CO_2 was directly dissociated into chemisorbed CO* and O* on the fcc-Co [31]. The CO* directly generated from CO_2 could be further hydrogenated to CH_4.

Combined with the above experimental results and literature, the Co-N-C single-atom and nanoparticle catalysts evidenced different reaction pathways. For the activation of CO_2, the Co-N_4 single-atom catalysts were more inclined to the H-assisted dissociation pathway to generate COOH*, while Co nanoparticle catalysts was more conducive to the direct dissociation of CO_2 to generate CO*. Furthermore, the adsorption strength of CO* was responsible for the selectivity of CO_2 hydrogenation. The Co-N-C single-atom catalysts basically did not adsorb CO, and CO generated by COOH* was directly desorbed. But the Co nanoparticle catalysts had strong affinity of CO* and was favorable to activate H_2, resulting in preferentially hydrogenation of CO* intermediates to CH_4 (Scheme 1).

3.4. Density functional theory Calculation

In order to further clarify the relationship between different Co species and the selectivity of CO and CH_4 during CO_2 hydrogenation, DFT calculation was employed to study the adsorption of key species and related elemental reaction mechanisms from CO_2 hydrogenation to CO and CH_4 on the Co-N_4 single-atom and Co-N-C nanoparticle catalysts. Two different Co catalyst models were constructed (Fig. S8). Fig. 6 provide a supplementary summary of the reaction mechanism based on DFT calculation. Fig. 6a-b shows the elemental reaction process for the
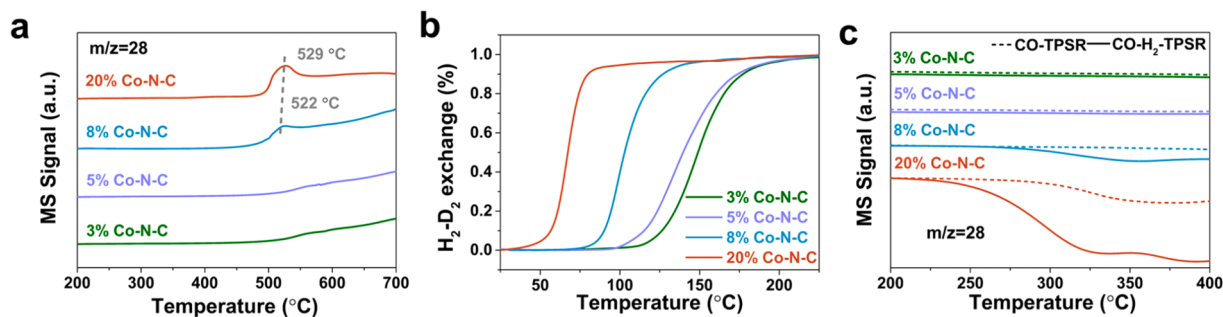

Fig. 4. (a) CO-TPD profiles over the Co-N-C catalysts; (b) H_2-D_2 exchange over the Co-N-C catalysts with different Co loadings; (c) CO-TPSR and CO-H_2-TPSR over the Co-N-C catalysts.
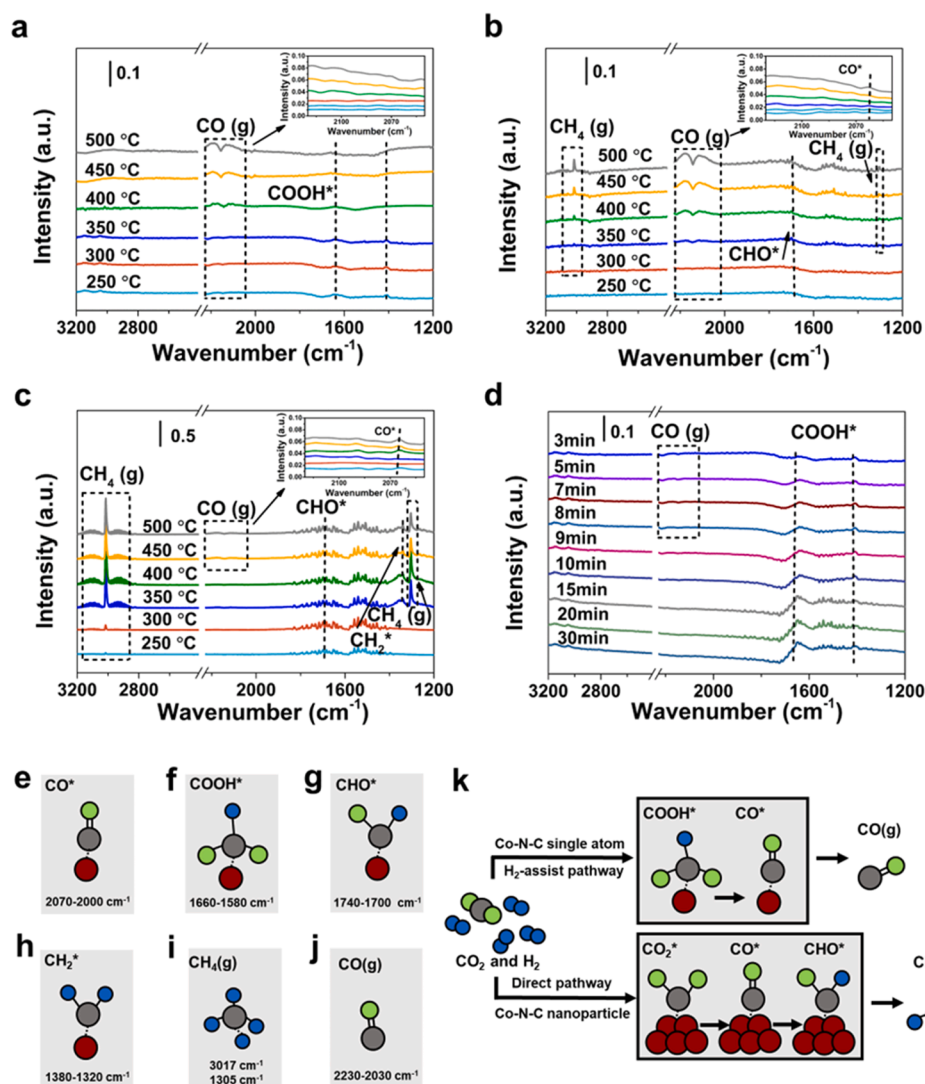
Fig. 5. In situ Diffuse reflectance infrared Fourier transform spectroscopy (DRIFTS) spectra of (a) 5% Co-N-C catalyst (b) 8% Co-N-C and (c) 20% Co-N-C after exposure to gas mixture ($H_2/CO_2/N_2 = 72/18/10$) in different temperature during CO_2 hydrogenation and (d) subsequent Ar purging of 5% Co-N-C catalyst. Adsorbed surface species with characteristic vibrational energies: (e) CO* , (f) COOH* , (g) CHO* , (h) CH_2 * , (i) CH_4 and (j) CO. (k) Simplified reaction pathway for single-atom cobalt catalyst in the RWGS reaction.
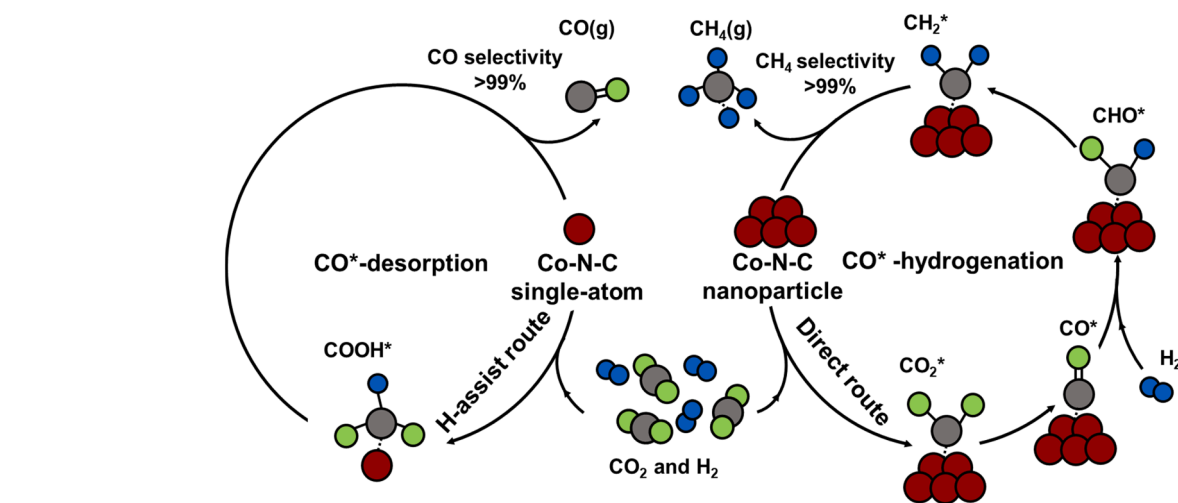
Scheme 1. Simplified reaction pathways for cobalt-catalyzed CO_2 hydrogenation. The direct dissociation route is generally considered to be the direct dissociation of CO_2 into the CO* intermediate, which can desorb or form CH* . H-assisted route typically involve surface carbonates, formates and acetates as intermediate species.
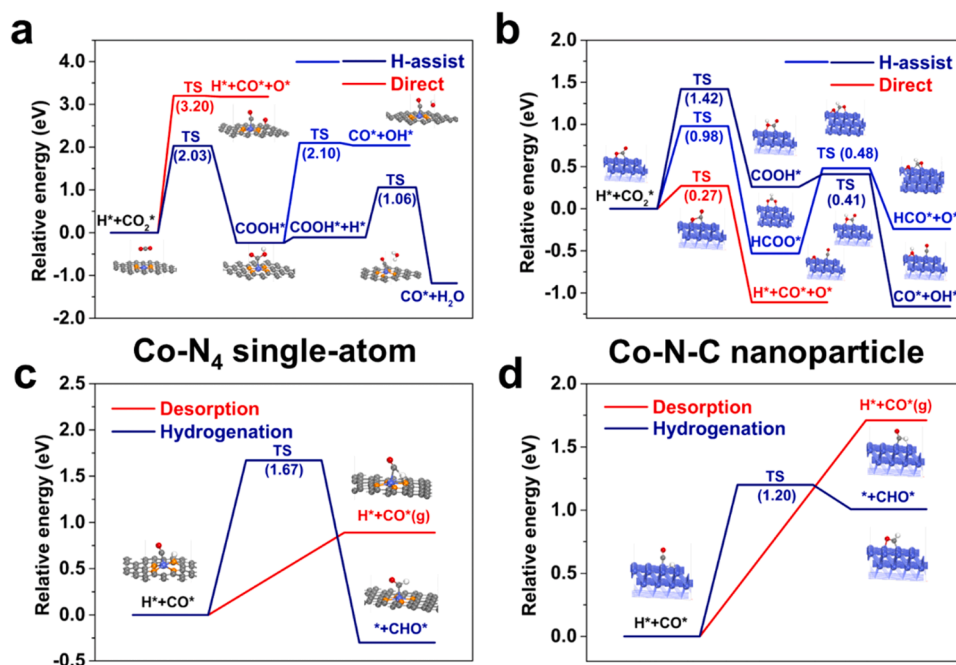
Fig. 6. Schematic representation of CO_2 hydrogenation reaction mechanism from (a) $Co-N_4$ single-atom and (b) Co-N-C nanoparticle. CO* activated dissociation pathway on (c) $Co-N_4$ single-atom and (d) Co-N-C nanoparticle.

hydrogenation of CO_2 to generate CO on the two catalyst models. For the single-atom $Co-N_4$ model, it is difficult to dissociate CO_2 directly, while H-assisted dissociation is relatively easier. For Co (111) nanoparticles, CO_2 could be directly dissociated, and H-assisted dissociation can also occur through hydrogenation to generate COOH* groups. Fig. 6c-d shows the comparison of the reaction processes of adsorbed CO* desorption and further hydrogenation between the two catalyst models. For the single-atom $Co-N_4$, the adsorbed CO has a lower energy barrier than further hydrogenation and CO desorption occurs preferentially. For Co (111) facet, barrier of the adsorbed CO further hydrogenation is lower than its desorption and the hydrogenation reaction of CO occur preferentially on the Co (111) facet. Meanwhile, the entire reaction process of CO further hydrogenation to generate CH_4 were calculated, and the results indicate that it is easy to generate CH_4 from CO hydrogenation, as well as the eventual desorption of CH_4 (Fig. S11). DFT calculation results are in well agreement with the product selectivity with different Co species obtained in CO_2 hydrogenation experiments. In addition, the adsorption energy values of CO*, CO_2*, CO* +H* and CO_2* +H* adsorbates on the two models are shown in Figs. S9 and 10.

Accordingly, atomically dispersed Co species are essential for CO formation during CO_2 hydrogenation reaction. Due to the weak strength of the adsorbed CO species and weak H_2 dissociation ability on atomically dispersed Co species, the adsorbed CO* will be directly desorbed into gaseous CO. On the other hand, CO* is more prone to further hydrogenation and different types of formyl and methyl were observed on Co nanoparticles (Fig. 6). For the activation of CO_2*, single atom Co catalysts prefer the H-assisted dissociation pathway while Co nanoparticle catalysts are more likely to directly dissociate CO_2. This observation is consistent with theoretical calculation (Fig. S10), which found that CO adsorption is strong (-1.71 eV $= -164.99$ kJ/mol) on Co nanoparticles and weak (-0.89 eV $= -85.87$ kJ/mol) on single atom Co.

4. Conclusions

In summary, we reported the atomically dispersed Co-N-C material with high-density and high cobalt loading (5%) for the first time.

Nitrogen could achieve charge transfer to adjust the electronic structure of the metal to make Co species form $Co^{\delta+}$ to further optimize the adsorption/desorption of intermediates. The catalyst displayed nearly 100% CO selectivity and remain 100 h stable during reverse water-gas shift reaction. Furthermore, the CO_2 conversion of 52.4% at 500 °C was close to equilibrium conversion and the CO STY reach up to 37.5 mol·kg^{-1}·h^{-1} at 500 °C, which has significantly improved compared with other Co catalysts. In comparison, 20% Co-N-C catalyst with Co nanoparticles exhibited high CH_4 selectivity up to 99%. CO-TPD showed that atomically dispersed Co has relative weak CO adsorbed ability, which favored CO formation and inhibited the formation of CH_4. And the H_2-D_2 exchange indicated that the Co nanoparticle has a stronger ability to activate H_2 than the single-atom Co, so it is more prone to hydrogenate the intermediate to CH_4. In situ DRIFTS demonstrated that the Co single-atom catalysts followed the H-assisted route to generate COOH* and further desorb to produce CO, while Co nanoparticle catalysts followed a direct dissociation route, which CO_2 firstly dissociated to CO* and further hydrogenated through CHO* and CH_2* intermediates to produce CH_4. And the dissociation path of CO_2 and the hydrogenation and desorption capacity of CO* were further confirmed by the DFT calculations, which were consistent with the experimental results. The results provide an efficient route for designing thermostable high-efficiency non-noble metal single-atom Co catalyst for RWGS reaction.

CRediT authorship contribution statement

Yihui Li: Investigation, Data curation, Conceptualization, Formal analysis, Methodology, Visualization, Writing - original draft. **Ziang Zhao:** Data curation, Supervision, Conceptualization, Writing - review & editing. **Wei Lu:** Data curation, Conceptualization, Writing - review & editing. **Hejun Zhu:** Project administration, Supervision, Validation, Writing - original draft. **Fanfei Sun, Bingbao Mei** and **Zheng Jiang:** Assistance in the experiment of EXAFS test and data processing. **Yuan Lyu:** Data curation, Formal analysis. **Xingkun Chen:** Data curation, Formal analysis. **Luyao Guo:** Data curation. **Tong Wu:** Data curation. **Xinzheng Ma:** Data curation. **Yu Meng:** Density functional theory calculations. **Yunjie Ding:** Supervision, Project administration, Writing -

review & editing.

Declaration of Competing Interest

The authors declare that they have no known competing financial interests or personal relationships that could have appeared to influence the work reported in this paper.

Data Availability

Data will be made available on request.

Acknowledgements

Appendix A. Supporting information

Supplementary data associated with this article can be found in the online version at doi:10.1016/j.apcatb.2022.122298.

References

[1] M.A.A. Aziz, A.A. Jalil, S. Triwahyono, A. Ahmad, CO₂ methanation over heterogeneous catalysts: recent progress and future prospects, Green. Chem. 17 (2015) 2647–2663.
[2] W. Gao, S. Liang, R. Wang, Q. Jiang, Y. Zhang, Q. Zheng, B. Xie, C.Y. Toe, X. Zhu, J. Wang, L. Huang, Y. Gao, Z. Wang, C. Jo, Q. Wang, L. Wang, Y. Liu, B. Louis, J. Scott, A.C. Roger, R. Amal, H. He, S.E. Park, Industrial carbon dioxide capture and utilization: state of the art and future challenges, Chem. Soc. Rev. 49 (2020) 8584–8686.
[3] B.B. Asare Bediako, Q. Qian, B. Han, Synthesis of C₂₊ Chemicals from CO₂ and H₂ via C-C Bond Formation, Acc. Chem. Res. 54 (2021) 2467–2476.
[4] M. He, Y. Sun, B. Han, Green carbon science: efficient carbon resource processing, utilization, and recycling towards carbon neutrality, Angew. Chem. Int. Ed. 61 (2022), e202112835.
[5] D. Xu, Y. Wang, M. Ding, X. Hong, G. Liu, S.C.E. Tsang, Advances in higher alcohol synthesis from CO₂ hydrogenation, Chem 7 (2021) 849–881.
[6] W. Wang, S. Wang, X. Ma, J. Gong, Recent advances in catalytic hydrogenation of carbon dioxide, Chem. Soc. Rev. 40 (2011) 3703–3727.
[7] W. Zhou, K. Cheng, J. Kang, C. Zhou, V. Subramanian, Q. Zhang, Y. Wang, New horizon in C1 chemistry: Breaking the selectivity limitation in transformation of syngas and hydrogenation of CO₂ into hydrocarbon chemicals and fuels, Chem. Soc. Rev. 48 (2019) 3193–3228.
[8] J. Artz, T.E. Muller, K. Thenert, J. Kleinekorte, R. Meys, A. Sternberg, A. Bardow, W. Leitner, Sustainable conversion of carbon dioxide: an integrated review of catalysis and life cycle assessment, Chem. Rev. 118 (2018) 434–504.
[9] M.T. Arslan, G. Tian, B. Ali, C. Zhang, H. Xiong, Z. Li, L. Luo, X. Chen, F. Wei, Highly selective conversion of CO₂ or CO into precursors for kerosene-based aviation fuel via an aldol-aromatic mechanism, ACS Catal. 12 (2022) 2023–2033.
[10] Y.P. Pei, J.X. Liu, Y.H. Zhao, Y.J. Ding, T. Liu, W.D. Dong, H.J. Zhu, H.Y. Su, L. Yan, J.L. Li, W.X. Li, High alcohols synthesis via Fischer-Tropsch reaction at cobalt metal/carbide interface, ACS Catal. 5 (2015) 3620–3624.
[11] W.L.Z. Zhao, R. Yang, H. Zhu, W. Dong, F. Sun, Z. Jiang, Y. Lyu, T. Liu, H. Du, Y. Ding, Insight into the formation of Co@Co₂C catalysts for direct synthesis of higher alcohols and olefins from syngas, ACS Catal. 8 (2018) 228–241.
[12] Y. Chen, J. Wei, M.S. Duyar, V.V. Ordomsky, A.Y. Khodakov, J. Liu, Carbon-based catalysts for Fischer-Tropsch synthesis, Chem. Soc. Rev. 50 (2021) 2337–2366.
[13] L. Zhong, F. Yu, Y. An, Y. Zhao, Y. Sun, Z. Li, T. Lin, Y. Lin, X. Qi, Y. Dai, L. Gu, J. Hu, S. Jin, Q. Shen, H. Wang, Cobalt carbide nanoprisms for direct production of lower olefins from syngas, Nature 538 (2016) 84–87.
[14] J.L.F. Jiao, X. Pan, J. Xiao, H. Li, H. Ma, M. Wei, Y. Pan, Z. Zhou, M. Li, S. Miao, J. Li, Y. Zhu, D. Xiao, T. He, J. Yang, F. Qi, Q. Fu, X. Bao, Selective conversion of syngas to light olefins, Science 351 (2016) 1065–1068.
[15] A.M. Bahmanpour, M. Signorile, O. Kröcher, Recent progress in syngas production via catalytic CO₂ hydrogenation reaction, Appl. Catal. B Environ. 295 (2021), 120319.
[16] M.D. Porosoff, B. Yan, J.G. Chen, Catalytic reduction of CO₂ by H₂ for synthesis of CO, methanol and hydrocarbons: Challenges and opportunities, Energy Environ. Sci. 9 (2016) 62–73.
[17] Q. Yi, W. Li, J. Feng, K. Xie, Carbon cycle in advanced coal chemical engineering, Chem. Soc. Rev. 44 (2015) 5409–5445.
[18] L. Shen, J. Xu, M. Zhu, Y.-F. Han, Essential role of the support for nickel-based CO₂ methanation catalysts, ACS Catal. 10 (2020) 14581–14591.
[19] M. Younas, L. Loong Kong, M.J.K. Bashir, H. Nadeem, A. Shehzad, S. Sethupathi, Recent advancements, fundamental challenges, and opportunities in catalytic methanation of CO₂, Energy Fuels 30 (2016) 8815–8831.
[20] M.M. Millet, G. Algara-Siller, S. Wrabetz, A. Mazheika, F. Girgsdies, D. Teschner, F. Seitz, A. Tarasov, S.V. Levchenko, R. Schlogl, E. Frei, Ni single atom catalysts for CO₂ activation, J. Am. Chem. Soc. 141 (2019) 2451–2461.
[21] Z. Zhao, M. Wang, P. Ma, Y. Zheng, J. Chen, H. Li, X. Zhang, K. Zheng, Q. Kuang, Z. X. Xie, Atomically dispersed Pt/CeO₂ catalyst with superior CO selectivity in reverse water gas shift reaction, Appl. Catal. B Environ. 291 (2021), 120101.
[22] Y. Jiang, Y. Sung, C. Choi, G. Joo Bang, S. Hong, X. Tan, T.S. Wu, Y.L. Soo, P. Xiong, M. Li, L. Hao, Y. Jung, Z. Sun, Single-atom molybdenum-N3 sites for selective hydrogenation of CO2 to CO, Angew. Chem. Int. Ed 61 (2022), e202203836.
[23] T. Fan, H. Liu, S. Shao, Y. Gong, G. Li, Z. Tang, Cobalt catalysts enable selective hydrogenation of CO₂ toward diverse products: recent progress and perspective, J. Phys. Chem. Lett. 12 (2021) 10486–10496.
[24] C. Vogt, E. Groeneveld, G. Kamsma, M. Nachtegaal, L. Lu, C.J. Kiely, P.H. Berben, F. Meirer, B.M. Weckhuysen, Unravelling structure sensitivity in CO₂ hydrogenation over nickel, Nat. Catal. 1 (2018) 127–134.
[25] A. Wang, J. Li, T. Zhang, Heterogeneous single-atom catalysis, Nat. Rev. Chem. 2 (2018) 65–81.
[26] J. Zheng, K. Lebedev, S. Wu, C. Huang, T. Ayvali, T.S. Wu, Y. Li, P.L. Ho, Y.L. Soo, A. Kirkland, S.C.E. Tsang, High loading of transition metal single atoms on chalcogenide catalysts, J. Am. Chem. Soc. (2021) 7979–7990.
[27] L.R. Winter, E. Gomez, B. Yan, S. Yao, J.G. Chen, Tuning Ni-catalyzed CO₂ hydrogenation selectivity via Ni-ceria support interactions and Ni-Fe bimetallic formation, Appl. Catal. B Environ. 224 (2018) 442–450.
[28] H. Xin, L. Lin, R. Li, D. Li, T. Song, R. Mu, Q. Fu, X. Bao, Overturning CO₂ hydrogenation selectivity with high activity via reaction-induced strong metal-support interactions, J. Am. Chem. Soc. (2022) 4874–4882.
[29] S. Kattel, P. Liu, J.G. Chen, Tuning selectivity of CO₂ hydrogenation reactions at the metal/oxide interface, J. Am. Chem. Soc. 139 (2017) 9739–9754.
[30] X. Chen, X. Su, H.Y. Su, X. Liu, S. Miao, Y. Zhao, K. Sun, Y. Huang, T. Zhang, Theoretical insights and the corresponding construction of supported metal catalysts for highly selective CO₂ to CO conversion, ACS Catal. 7 (2017) 4613–4620.
[31] W. Li, X. Nie, H. Yang, X. Wang, F. Polo-Garzon, Z. Wu, J. Zhu, J. Wang, Y. Liu, C. Shi, C. Song, X. Guo, Crystallographic dependence of CO₂ hydrogenation pathways over HCP-Co and FCC-Co catalysts, Appl. Catal. B Environ. 315 (2022), 121529.
[32] W. Li, X. Nie, X. Jiang, A. Zhang, F. Ding, M. Liu, Z. Liu, X. Guo, C. Song, ZrO₂ support imparts superior activity and stability of Co catalysts for CO₂ methanation, Appl. Catal. B Environ. 220 (2018) 397–408.
[33] W. Li, G. Zhang, X. Jiang, Y. Liu, J. Zhu, F. Ding, Z. Liu, X. Guo, C. Song, CO₂ hydrogenation on unpromoted and M-promoted Co/TiO₂ Catalysts (M = Zr, K, Cs): effects of crystal phase of supports and metal-support interaction on tuning product distribution, ACS Catal. 9 (2019) 2739–2751.
[34] I.C.T. Have, J.J.G. Kromwijk, M. Monai, D. Ferri, E.B. Sterk, F. Meirer, B. M. Weckhuysen, Uncovering the reaction mechanism behind CoO as active phase for CO₂ hydrogenation, Nat. Commun. 13 (2022) 324.
[35] H. Liang, B. Zhang, P. Gao, X. Yu, X. Liu, X. Yang, H. Wu, L. Zhai, S. Zhao, G. Wang, A.P. van Bavel, Y. Qin, Strong Co-O-Si bonded ultra-stable single-atom Co/SBA-15 catalyst for selective hydrogenation of CO₂ to CO, Chem. Catal. 2 (2022) 610–621.
[36] N.H.M.D. Dostagir, R. Rattanawan, M. Gao, J. Ota, J.Y. Hasegawa, K. Asakura, A. Fukouka, A. Shrotri, Co single atoms in ZrO₂ with Inherent oxygen vacancies for selective hydrogenation of CO₂ to CO, ACS Catal. (2021) 9450–9461.
[37] Z. Xia, H. Zhang, K. Shen, Y. Qu, Z. Jiang, Wavelet analysis of extended X-ray absorption fine structure data: Theory, application, Phys. B 542 (2018) 12–19.
[38] G. Kresse, Efficient iterative schemes for ab initio total-energy calculations using a plane-wave basis set, Phys. Rev. B 54 (1996) 11169–11186.
[39] P.E. Blochl, Projector augmented-wave method, Phys. Rev. B 50 (1994) 17953–17979.
[40] K.B.J.P. Perdew, M. Ernzerhof, Generalized gradient approximation made simple, Phys. Rev. Lett. 77 (1996) 3865–3868.
[41] J.H.G. Kresse, First-principles study of the adsorption of atomic H on Ni (111), (100) and (110), Surf. Sci. 459 (2000) 287–302.
[42] P.U.G. Henkelman, H. Jonsson, A climbing image nudged elastic band method for finding saddle points and minimum energy paths, J. Chem. Phys. 113 (2000) 9901–9904.
[43] L. Zhao, Y. Zhang, L.B. Huang, X.Z. Liu, Q.H. Zhang, C. He, Z.Y. Wu, L.J. Zhang, J. Wu, W. Yang, L. Gu, J.S. Hu, L.J. Wan, Cascade anchoring strategy for general mass production of high-loading single-atomic metal-nitrogen catalysts, Nat. Commun. 10 (2019) 1278.
[44] Z. Zhao, W. Lu, H. Zhu, W. Dong, Y. Lyu, T. Liu, X. Chen, Y. Wang, Y. Ding, Tuning the Fischer-Tropsch reaction over CoₓMnᵧLa/AC catalysts toward alcohols: effects of La promotion, J. Catal. 361 (2018) 156–167.

[45] H. Qi, J. Yang, F. Liu, L. Zhang, J. Yang, X. Liu, L. Li, Y. Su, Y. Liu, R. Hao, A. Wang, T. Zhang, Highly selective and robust single-atom catalyst Ru1/NC for reductive amination of aldehydes/ketones, Nat. Commun. 12 (2021) 3295.

[46] Z. Zhao, W. Lu, C. Feng, X. Chen, H. Zhu, R. Yang, W. Dong, M. Zhao, Y. Lyu, T. Liu, Z. Jiang, Y. Ding, Increasing the activity and selectivity of Co-based FTS catalysts supported by carbon materials for direct synthesis of clean fuels by the addition of chromium, J. Catal. 370 (2019) 251–264.

[47] J. Li, C. Li, S. Feng, Z. Zhao, H. Zhu, Y. Ding, Atomically dispersed Zn-N_x sites in N-doped carbon for reductive N-formylation of nitroarenes with formic acid, ChemCatChem 12 (2020) 1546–1550.

[48] C. Wang, E. Guan, L. Wang, X. Chu, Z. Wu, J. Zhang, Z. Yang, Y. Jiang, L. Zhang, X. Meng, B.C. Gates, F.S. Xiao, Product selectivity controlled by nanoporous environments in zeolite crystals enveloping rhodium nanoparticle catalysts for CO_2 hydrogenation, J. Am. Chem. Soc. 141 (2019) 8482–8488.

[49] T. Herranz, X. Deng, A. Cabot, J. Guo, M. Salmeron, Influence of the cobalt particle size in the CO hydrogenation reaction studied by in situ X-ray absorption spectroscopy, J. Phys. Chem. B 113 (2009) 10721–10727.

[50] L.F. Bobadilla, J.L. Santos, S. Ivanova, J.A. Odriozola, A. Urakawa, Unravelling the role of oxygen vacancies in the mechanism of the reverse water-gas shift reaction by operando DRIFTS and ultraviolet-visible spectroscopy, ACS Catal. 8 (2018) 7455–7467.